Int. J. Electrochem. Sci., 10 **(2015)** 10524 - 10542

International Journal of
ELECTROCHEMICAL
SCIENCE
www.electrochemsci.org

Physical and Electrochemical Characteristics of Carbon Monoliths Electrodes from Activation of Pre-carbonized Fibers of Oil Palm Empty Fruit Bunches Added with Varying Amount of Polypyrrole

S. Soltaninejad[1], Rusli Daik[1], M. Deraman[2], Y. C. Chin[2], N. S. M. Nor[2], N. E. S. Sazali[2], E. Hamdan[2], M. R. M. Jasni, M. M. Ishak[2], M. Noroozi[2], M. Suleman[2]*

[1]School of Chemical Sciences and Food Technology, Universiti Kebangsaan Malaysia, 43600 Bangi, Selangor, Malaysia
[2]School of Applied Physics, Faculty of Science and Technology, Universiti Kebangsaan Malaysia, 43600 Bangi, Selangor, Malaysia
[*]E-mail: madra@ukm.edu.my (corresponding author)

Received: 25 May 2015 / *Accepted:* 17 September 2015 / *Published:* 4 November 2015

Fibres of oil palm empty fruit bunches (OPEFB), a large quantity waste material generated at palm oil mills, were converted into self-adhesive carbon grains (SACG). KOH treated SACG were added with 0, 5, 10, 15 and 20 wt. % of polypyrrole (PPy) to produce green monoliths (GMs) which were used to obtain activated carbon monoliths (ACMs) electrodes via carbonization (N_2 environment) and activation (CO_2 environment) for their application in symmetrical supercapacitors. Various properties of the electrode materials were examined by thermo-gravimetric analysis, X-ray diffraction and field emission scanning electron microscopy techniques. Electrochemical performance of the ACMs as electrodes was tested with 1 M H_2SO_4 as electrolyte using electrochemical impedance spectroscopy, cyclic voltammetry and galvanostatic charge-discharge techniques. Addition of (15-20) wt. % of PPy in GMs affects the structure, microstructure and pore structure of the ACMs and consequently leads to an enhancement of ~ (20-50) F g^{-1}, ~ 3-6 Wh kg^{-1} and ~ 96-98 W kg^{-1} in specific capacitance (C_{sp}), specific energy (E) and specific power (P), respectively, with respect to the electrode prepared from GMs without PPy which offers corresponding values of ~ (2-10) F g^{-1}, 2 Wh kg^{-1}, and 87 W kg^{-1}.

Keywords: Self-adhesive carbon grains; Polypyrrole; Activated carbon monoliths electrodes; Physical property; Symmetrical supercapacitors; Supercapacitive performance.

1. INTRODUCTION

Supercapacitors (also referred as electrochemical capacitors or ultracapacitors) owing to their exceptional properties including, high specific capacitance, rapid charge-discharge rate, long cycle life, improved safety, simple principle of operation etc., have attracted tremendous attention. These are the energy storage devices particularly, having higher specific energy than conventional capacitors and higher power density and longer cycle life than rechargeable batteries [1-4]. Due to these extraordinary features they are used in various applications such as portable consumer electronics, hybrid electric vehicles, computer memory backup systems and large industrial energy and management [2].

Different categories of the electrode materials such as porous carbons, transition metal oxides or electrically conducting polymers, or a combination of these determine the energy storage mechanism in supercapacitors and hence the type of supercapacitors produced [1]. If electrodes are made of porous carbon, supercapacitors are known as electric double layer capacitors (EDLCs), where the capacitance arises from the electrostatic charge accumulation by means of reversible ion absorption at the electrode/electrolyte interface (non-faradaic process) [1]. Because of the fast and near surface charge accumulation, the EDLCs offer excellent power delivery and high degree of reversibility leading to the long cycle life (~ 10^6 charge-discharge cycles) [5-7]. For electrodes made of transition metal oxides or electrically conducting polymers, the supercapacitors are known as psuedocapacitors in which the capacitance relies on fast and reversible redox reactions (faradaic processes) occurring at the surface of electroactive materials [8]. Using the electrodes from both classes, these two charge storage mechanisms can act simultaneously and the resulting configuration is called hybrid supercapacitors.

The advent of new techniques and discovery of novel electrode materials play an important role in determining the performance of supercapacitors. As cited above the electrode materials that are commonly used in supercapacitors include carbon-based materials available in variety of forms (carbon powders/fibers/aerogels/composites/sheets/monoliths/tubes etc., to carbon nanotubes and graphene), transition metal oxides and conducting polymers, such as polyaniline and polypyrrole (PPy) [9-12]. High surface area activated carbons, due to their attractive properties such a slow cost, high conductivity, ease of processing, controlled porosity, relatively inert electrochemistry, etc., have been investigated most widely as electrode materials [6]. In this race, the activated carbons, derived particularly from biomass precursors such as coconut shell, fruit shells, wood, bunches etc. are cheaper, readily available, environmentally friendly, renewable, and structurally porous hence preferred to prepare electrodes for supercapacitors [13-20]. By changing the activation process or type of precursor the porosity of the activated carbons can be tailored to the desired pore size distribution [21, 22, 16].

Various properties of the electrode materials such as conductivity, SSA, pore size distribution, wettability that facilitate ions to access the bulk of electrode have a significant effect on the performance of the EDLCs [17]. Theoretically, there should be a proportional increase in specific capacitance with specific surface area (SSA). However, due to the molecular sieving effect not all the micropores are accessible to the ions that results in the decrease of effective surface area exposed to the ions and hence a significant deviation from this simple law is generally observed [23]. Therefore, for activated carbons, only about 10-20 % of the theoretical capacitance is observed [18].

Recently, PPy has been used as a synthetic precursor (that may leave high percentage of carbonaceous residue after thermal treatment) to obtain activated carbon offering one of the highest specific surface areas (> 3400 m^2g^{-1}) that have ever been reported for the carbon based materials in the literature [9]. With this carbon based electrode using PTFE as a binder and ionic liquid, 1-ethyl-3-methyl imidazolium tetrafluoroborate ($EMImBF_4$) as an electrolyte a specific capacitance value of ~ 300 Fg^{-1} at an elevated temperature ~ 60^oC has been demonstrated [9]. However, use of binder like PVdF-HFP, PTFE etc., in general, decreases the porosity/SSA and conductivity of the carbon based electrodes. Also the excessive increment in area results in the decrease of the conductivity of the carbon materials [24].

In this report, we present a totally different route to prepare ACMs electrodes without binder from the primary precursor GMs added with varying amounts of PPy acting as an additive (or a secondary precursor) prior to the carbonization and activation of the GMs. The precursor GMs was prepared from SACG (processed from the pre-carbonized fibres of oil palm empty fruit bunches). In order to investigate the effect of PPy addition (in GMs) on the physical and electrochemical properties of the ACMs, the contents of PPy was varied from 0 to 20 % by weight. The performance of supercapacitor cells with modified electrodes was found to be enhanced substantially in terms of its specific capacitance (C_{sp}), specific energy (E) and specific power (P).

2. EXPERIMENTAL PART

2.1.1 Oil Palm Empty Fruit Bunches

Oil palm empty fruit bunches (OPEFB) used in the present study were purchased from the Ecofibre Technology Sdn. Bhd. OPEFB from oil palm tree (Elaeisguineensis) is a by-product produced in a large quantity at the palm oil mills. From the 370 oil palm mills operating in year 2003, it was estimated that an average of 19 tonnes/hectares of fresh fruit bunches was produced [25, 26]. Based on 23 % extraction, around 4.4 tonnes of OPEFB was produced per hectares in the year 2003 throughout Malaysia. The properties of OPEFB can be summarized as follows [27]: (a) OPEFB comprise of fibres or bundles of fibers that are stringy and flexible, (b) the mass fractions of fresh OPEFB are of 34 % dry matter and 3 % oil and 63 % water and represents approximately 20-22 % of the weight of fresh fruit bunches. OPEFB contain a ligno-cellulosic natural polymer material with the mass fraction of 45-50 % cellulose, 25-35 % hemicellulose and 25-35 % lignin, and (c) in the dry form, the mean mass fraction percentages of chemical composition are as follows: ash (6.3), oil (8.9), C (42.8), N2 (0.8), P2O5 (0.22), K2O (2.9), MgO (0.3) and CaO (0.25) [28].

2.1.2 Polypyrrole (PPy)

PPy is a type of organic polymer formed by polymerization of pyrrole with the formula C_4H_4NH. It is a colour less volatile liquid that readily turns into dark material upon exposure to air. PPy and related conductive polymers have two main applications in electronic devices and chemical sensors [10]. PPy offers a greater degree of flexibility in electrochemical processing than most conducting polymers, and consequently the material has been the subject of much research interest as a supercapacitor or battery electrodes [11, 12]. In our work, the PPy was prepared from the purified monomer pyrrole. The purification was done twice, i.e. by allowing the monomer pyrrole to pass through a column filled with Al_2O_3 (Alumina) and wool glass for 1 to 2 h.

The process of preparing PPy involves four steps:

i. Preparing the solution of ammonium persulfate oxidant (APS) (45.64 g of the APS dissolved in 200 ml deionized water for 30 min).
ii. Pouring the achieved purified pyrrole in reaction flask which was kept at (0-5) °C.
iii. Adding the solution drop wise for 1 h in reaction flask.
iv. The mixture was stirred for 4 h from the beginning.

In the final step, black mixture of PPy was obtained and then poured into 600 ml methanol and after 24 h, the mixture was filtered and washed with distilled water, and subsequently after 48 h it was dried in a vacuum oven at 40°C for 8 h. Finally, around 3 g black powder of PPy was obtained.

2.2 Electrode Preparation and Cell Fabrication

Using the previously developed procedure of electrode and supercapacitor cell to produce carbon from fibers of OPEFB, these fibers were processed to SACG by low temperature (280°C) pre-carbonization (Furnace CTMSB46). The SACG with powder particle size less than or equal to 106 μm were prepared by grinding (300-500 μm hole size filters), 18 h of ball-milling (ball mill AC Motor BS 500-110) and sieving (Matest 24030 Brembate Sopra (BG). The SACG was found to exhibit a satisfactory binding of particles in the GM [29, 30]. The mixture (95 wt. % SACG treated with 5 wt. % KOH) was prepared as follows: 60.0 g SACG and 3.0 g of KOH (5 wt. %) was poured into 630 ml boiling water; stirred for 1 h and followed by drying in an oven at 100°C for 48 h. The dried mixture weighing approximately 10 g was milled for 20 min to obtain a homogeneous composition. The mixtures of SACG and PPy were prepared with different weight percentages of PPy, i.e. 0, 5, 10, 15 and 20 wt. %, respectively.

For each composition, the mixture with the weight as shown in Table 1 was processed into GMs using a press pelletizing machine (VISITEC 2009-Malaysia). The compression pressure and mold diameter were 250 kg cm^{-2} and 20 mm respectively. The GMs were carbonized into carbon monoliths (CMs: CM00, CM5, CM10, CM15 and CM20) using a carbonization furnace (Vulcan Box Furnace 3-1750) under a 1.5 L min^{-1} flow of N_2 gas, up to 800°C. In this experiment, our previous multi-step was employed [21].

ACM00, ACM05, ACM10, ACM15 and ACM20 were produced by a physical activation from these respective CMs via CO_2 (1.0 L min^{-1}) activation at 800°C for 3 h with a heating rate of 5°C min^{-1}. After polishing to a thickness of 0.4mm, the ACMs were extensively washed with distilled water until reaching pH 7 [13]. The polished ACMs were used as electrodes in supercapacitor cells using 316L stainless steel (0.02 mm thick) as current collector, 1 M H_2SO_4 as electrolyte and a 25 μm thickness of microporous membrane (Celgard, LLC) as a separator. The cells fabrication was made according to the procedure reported previously [14].

2.3 Physical Characterizations`

The monoliths thickness and diameter were measured using digital Vernier Calliper (Mitutoyo 193-253) and the masses of the monoliths samples were measured using weighing balance (Mettler Toledo AB204). The density of the samples was then determined using these measured data. The thermal decomposition behavior of the SACG and mixtures of SACG and PPy were investigated using thermo-gravimetry instrument (Mettler Toledo TGA/SDTS 851). X-ray diffractometer (XRD) (Bruker AXS D8) employing Cu-K-alpha radiation with a wavelength of 1.5406 Å and selected for scanning over the angular range 2θ from 0° to 70° [31] was used to determine the structure of the ACMs. The field emission scanning electron microscope (FESEM) (Supra PV 55 model) was employed to study the morphology of the fractured ACMs. N_2 adsorption-desorption isotherm measurements at 77 K were carried out to find the porosity of the ACMs using an accelerated surface area porosimeter system (ASAP 2010 Micromeretics). The FTIR instrument, Spectrum GX FTIR Spectrometer (The Perkin-Elmer Corporation 761 Main Avenue Norwalk, CT 06859-0240) along with MID IR source of radiation comprising of a ceramic body containing a special packing material surrounding the heating element was employed to probe the structure of the ACMs. Various porosity parameters including average pore diameter (D), S_{BET} (the BET surface area), S_{micro} (surface area due to micro-pores), S_{meso} (surface area due to meso-pores), V_{meso} (volume due to meso-pores), V_{micro} (volume due to micro-pores) etc. were determined from the N_2 adsorption-desorption isotherm data using ASAP 2020 software and the standard formalism [32].

2.4 Electrochemical Characterization

Various physical techniques such as electrochemical impedance spectroscopy (EIS), cyclic voltammetry (CV) and galvanostatic charge-discharge (GCD) were used to test the supercapacitor cells. An electrochemical instrument-interface (Solartron SI 1286 and Solartron 1255HF Frequency Response Analyser) was employed to carry out the experiments at room temperature (25 °C).

The C_{sp} of the supercapacitor cell was evaluated from EIS data using the relation:

$$C_{sp} = -\frac{1}{2\pi f_l Z''_l m} \tag{1}$$

where f_l is the lowest frequency, Z''_l is the imaginary impedance at f_l and m is the mass of the single electrode.

Following relations have been used to plot the C_{sp} as a function of the frequency:

$$C(\omega) = C'(\omega) - jC''(\omega) \tag{2}$$

$$C''(\omega) = \frac{Z'(\omega)}{w\,|Z(\omega)|^2} \tag{3}$$

$$C'(\omega) = -\frac{Z''(\omega)}{w\,|Z(\omega)|^2} \tag{4}$$

where Z(ω) is equal to $\frac{1/}{j\omega C(\omega)'}$, $C'(\omega)$ is the real capacitance, $C''(\omega)$ is the imaginary capacitance, Z'(ω) is the real impedance and Z''(ω) is the imaginary impedance [33].

From the voltammograms, the C_{sp} of the supercapacitor cell was determined using equation:

$$C_{sp} = \frac{2i}{Sm} \tag{5}$$

where i is the electric current, S is the scan rate and m is the mass of the single electrode.

From the GCD data (charge-discharge curve) recorded at a selected current density, the C_{sp} of the electrodes was determined using equation:

$$C_{sp} = -\frac{2i'}{m}\left(\frac{\Delta t}{\Delta V}\right) \quad (6)$$

Where i' is the discharge current, ΔV is the voltage and Δt is the discharge time [15, 16].
The values of the P and E were also calculated from the GCD data using the following equations:

$$P = \frac{Vi}{m} \quad (7)$$

$$E = \frac{Vit}{m} \quad (8)$$

where i is the discharge current, V is the voltage (excluding the iR_{drop} occurring at the beginning of the discharge) and t is the time [17, 18, 23].

3. RESULTS AND DISCUSSION

3.1. Physical Properties

3.1.1 Weight, Dimension and Density

The masses (m), thicknesses (t) and diameters (d) of the GMs and ACMs were measured and analysed, and their densities were calculated from these data (Table 1). It was found that after activation the percentage of weight loss and diameter shrinkage systematically decreased with increasing PPy content in the samples. It can be estimated from this table that the samples underwent 0.60 % to 0.63 % weight loss and 24 % to 28 % volume shrinkage after activation. These effects are due to the release of the non-carbon material and reorganization of the carbon atoms throughout the carbonization and activation processes. A small difference between the weight loss and dimensional shrinkage percentages has been observed elsewhere [21, 33] and is a major factor contributing to the small differences in the sample densities before and after carbonization [19].

Table 1. Mass, dimension and density of the GMs and ACMs

GM00	1.17	2.824	20.058	1.33
GM05	1.17	2.895	20.059	1.32
GM10	1.17	2.917	20.058	1.30
GM15	1.17	2.924	20.093	1.30
GM20	1.17	2.953	20.089	1.32
ACM00	0.43	2.010	14.422	1.32
ACM05	0.44	2.069	14.461	1.28
AC	0.44	2.181	14.607	1.27

M10				
AC M15	0.45	2.109	15.129	1.20
AC M20	0.46	2.115	15.189	1.26

3.1.2 Thermo-gravimetric Analysis (TGA)

Figure 1 shows the (TGA) curves for GM00, GM10 and GM20 electrodes over a temperature ranging from 25 °C to 600 °C. As expected, all the curves are very similar (Figure 1). It can be observed that a marginal weight loss occurs up to 100°C which is mainly caused by the evaporation of moisture. The TGA result of the GM00 is similar to that reported earlier for the SACG [28], and wood [35]. Thermal decomposition of lingo cellulosic materials such as biomass is in general indicated by weight loss beginning at 200 °C when the hemicellulose component begins to break down. The loss in weight rapidly increases above 200 °C, as hemicellulose decomposes, above 200 °C, and reaches a maximum at 300 °C, where apart from the cellulose, lignin also decomposes. At that temperature the cellulose has already decomposed while the lignin components continue to break down. By 360 °C there is a 70 % loss in weight, but lignin decomposition continues. Further heat treatment to 600 °C yielded 21 wt. % solid carbons [35].

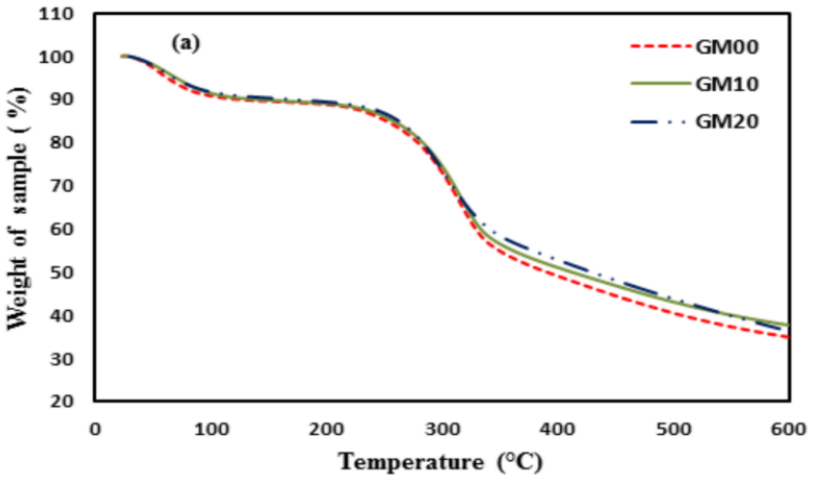

Figure 1. TGA curves for the GM00, GM10 and GM20 electrodes.

3.1.3 X-ray Diffraction

Figure 2 (a) shows the X-ray diffractograms for the GM00, GM10 and GM20 samples. The diffraction peaks, namely the (002)-peak at 2θ about 22.6°, and the composite of (101)- and ($10\bar{1}$)-peaks at 2θ about 15.4° are typically due to the cellulose component in the SACG, whose structure does not collapse during the pre-carbonisation process of OPEFB fibres up to the temperature of 280 °C [28]. The broadening of the composite peak does not change with the change of PPy content in the GMs, but the (002)-peak broadening appears to decrease slightly with the increasing PPy content in the

GMs. The reason for this behavior is that the intensity of broad diffraction peak at ~25° belongs to PPy, which is higher for higher PPy content in the GMs, contribute to such a broadening [36].

It can be observed from the XRD patterns (Figure 2 (b)) that the structure of all ACMs **(**ACM00, ACM05, ACM10, ACM15 and ACM20) electrodes is semi-crystalline which can be explained by a turbostratic structure model. The presence of two broad peaks due to (002) and (100) diffraction planes at 2θ approximately 25° and 44°, respectively, show that all the ACMs have turbostratic structure; similar results for the ACMs prepared from OPEFB fibres were reported previously [21]. It was expected that such a turbostratic structure would be typically exhibited by carbon derived from biomass [27, 13].

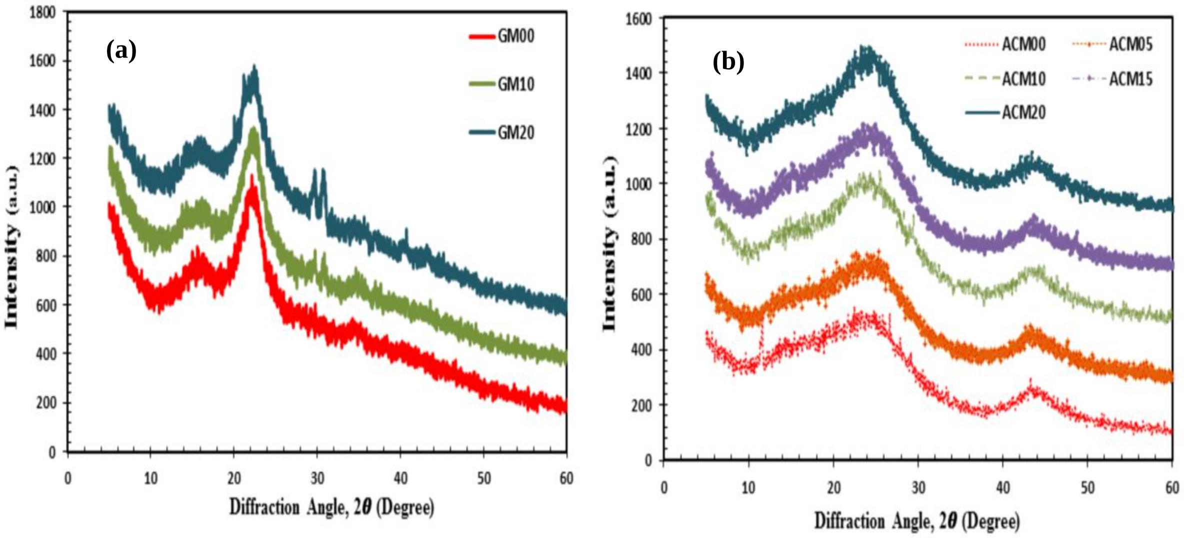

Figure 2. X-ray diffraction patterns for (a) GM00, GM10 and GM20 electrodes, and (b) ACM00, ACM05, ACM10, ACM15 and ACM20 electrodes.

The values of various structural parameters (shown in Table 2) i.e., the interlayer spacing, d_{002} and d_{100}, and microcrystallite dimensions, L_c (stack height) and L_a (stack width) of the ACMs were obtained the following procedure. The values of d_{002} and d_{100} were calculated using Bragg's equation ($n\lambda = 2d\sin\theta$, where $n = 1$, λ is the wave length (1.5406 Å) of the X-ray radiation and θ is the Bragg angle representing the position of the (002) and (100) diffraction peaks). The values of L_c and L_a were determined from the (002) and (100) peaks, respectively. The calculation was done using the Debye-Scherrer equation ($L_{c,a} = K\lambda / \beta_{c,a} \cos\theta$, where K is the shape factor equal to 0.89 and 1.84 for L_c and L_a, respectively, and $\beta_{c,a}$ is the full width at half maximum of the symmetrically shaped diffraction peaks) [28, 37, 38].

It can be noticed from Table 2 that the change in the d_{002} and d_{100} values is very small and it follows no systematic trend with the increase of the weight percentage of PPy. Similar behavior is exhibited by the values of the microcrystallite dimensions L_c and L_a of the ACMs. These results can further be analyzed by calculating ratios of L_c/L_a and L_c/d_{002} which respectively represent the relative density of planes in the microcrystallites and the mean number of edge and basal planes in the microcrystallites of the ACMs. The relative density of edge and basal planes can represent the edge orientation of the micro-crystallites. The ratios (L_c/L_a and L_c/d_{002}) shown in Table 2 indicate that only 15-20 wt. % addition of PPy causes them to change noticeably. This implies that an adequate amount of PPy addition to SACG can promote thicker microcrystallites and also more number of graphitic-like planes in the microcrystallites of ACMs during the activation process; possibly due to increasing effect resulted from their difference in thermal degradation property of the SACG and PPy composite. The values of these ratios are comparable to those reported elsewhere [17, 21].

Table 2. Structural parameter for ACM00, ACM05, ACM10, ACM15 and ACM20

ACM00	2.0399	3.7387	8.330	30.513	0.273	2.227
ACM05	2.0351	3.8434	7.311	27.693	0.264	1.903
ACM10	2.0460	3.7799	7.761	25.870	0.300	2.053
ACM15	2.0156	3.6800	9.413	24.641	0.382	2.558
ACM20	2.0310	3.7204	9.334	26.000	0.359	2.509

3.1.4 Field Emission Scanning Electron Microscopy

The FESEM analysis was done to investigate how the microstructure of the ACMs gets affected with the addition of PPy in GMs. The FESEM micrographs of the ACM00, ACM10 and ACM20 electrodes recorded at low magnification and at high magnification are shown in Figure 3 ((a), (b), (c)) and ((d), (e), (f)), respectively. These micrographs show the porous characteristics of the ACMs electrodes. It can be observed in Figure 3 that the images at this level of low magnification (1,000 X) show no obvious difference in the microstructure of the ACMs electrodes prepared from the GMs added with different amount of PPy. From Figure 3 (d), (e) and (f), it is clear that a typically cauliflower-like spherical shape of pores are observed, that is, similar to those reported for activated carbon samples [33]. Actually the changes in the surface morphology of the electrodes occur at microporosity level and hence are not observable at a magnification level (100,000 X) corresponding to a much lower scale of ~ 200 nm.

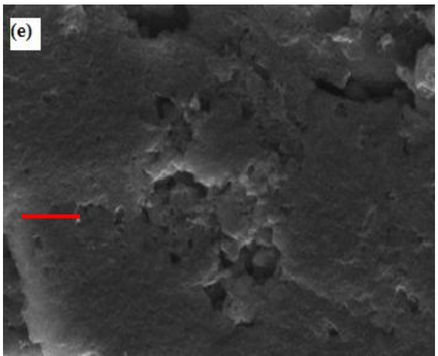

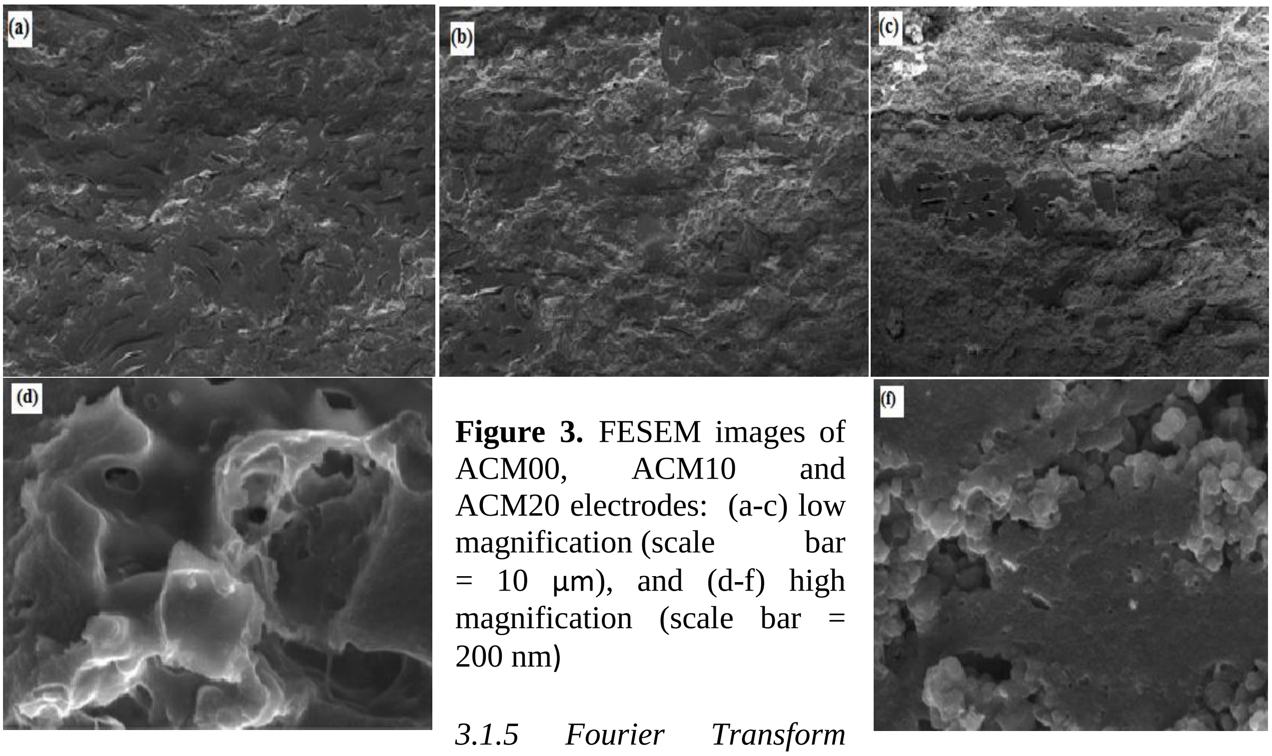

Figure 3. FESEM images of ACM00, ACM10 and ACM20 electrodes: (a-c) low magnification (scale bar = 10 μm), and (d-f) high magnification (scale bar = 200 nm)

3.1.5 Fourier Transform Infrared Spectroscopy

The FTIR spectra of the GM00, GM10 and GM20 are shown in Figure 4 (a). The spectra show the bands or peaks for various surface functional groups. The wide peak appearing at around ~3350 cm^{-1} is typically attributed to hydroxyl groups or adsorbed water. The band located at ~2940 cm^{-1} represents the C–H stretching vibrations in methyl and methylene groups [39]. The band at 2362 cm^{-1} can be ascribed to C=C stretching vibrations in alkyne groups, which normally appears when there is a release of light volatile matters during the heating process [40] and this result was reasonably expected because the fibers were subjected to the heating or pre-carbonization before they were ground and milled. The band appearing at ~1740 cm^{-1} corresponds to carbonyl (C=O) groups. The olefinic C=C stretching vibrations adsorptions produce the band at ~1620 cm^{-1} while the skeletal C=C vibrations in aromatic rings produce another two bands at ~ 1520 and ~1420 cm^{-1}. The bands at ~1460 and ~1371 cm^{-1} are ascribed to the C–H in-plane bending vibrations in methyl and methylene groups. A relatively intense band at ~1060 cm^{-1} is associated with C–O stretching vibrations in alcohols, phenols, or ether or ester groups. The C–H out-of-plane bending vibrations in benzene derivative correspond to the bands at ~897 cm^{-1}. Finally, the band associated with the O–H out-of-plane bending vibrations band is observed at ~615 cm^{-1}. From the band assignment, the oxygen groups present in the GMs include carbonyl groups, ethers, esters, alcohols, and phenol groups.

The FTIR spectra of ACMs shown in Figure 4 (b) having various functional groups with their respective bands are different from that shown in Figure 4 (a), and which implies that the surface functional groups of the GMs experienced chemical changes during activation. For example, the band at ~2940 cm^{-1} (the C–H vibrations in methyl) shown in Figure 4(a) is no longer appearing in Figure 4(b), indicating that the samples had gone through an almost complete carbonization and activation [40]. A very small change is observed for the band at ~ 2362 cm^{-1}, which can be ascribed to $C\equiv C$ stretching vibrations in alkyne groups. The peak at ~1700 cm^{-1}, which is not observed in the GMs, belonging to carbonyl groups, appears in the ACMs. The band occurring at ~1320 cm^{-1} can be attributed to C–O stretching vibrations in carboxylate groups [10]. It can also be seen in Figure 4(b); bands underwent change in their intensity and position due to the addition of the PPy in the GMS, which is indirectly indicating that there would be a change in the surface functionality of the electrodes prepared from the GMs containing PPy.

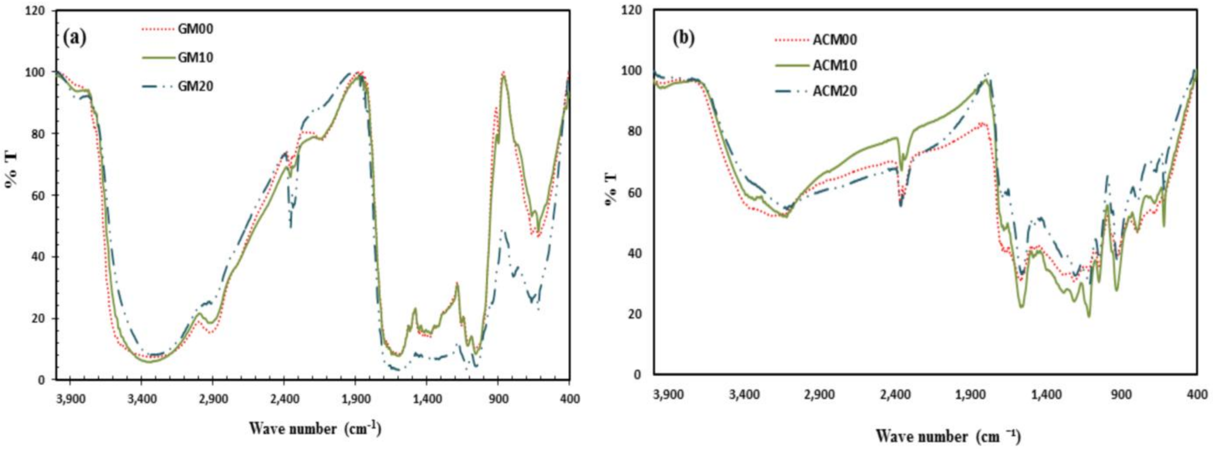

Figure 4. FTIR spectra of GM00, GM10 and GM20 electrodes.

3.1.6 Nitrogen Adsorption and Desorption

The nitrogen adsorption-desorption isotherm data for all the compositions of ACMs were evaluated and it was found that the ACMs prepared from GMs containing appropriate amount of PPy possess the pore structure and networks that can facilitate efficient diffusion of electrolyte ions into pores in electrodes. It was further found that the electrodes ACM15 and ACM20, have S_{meso}/S_{BET} ratios ~1.12 and 1.19 and average pore diameters ~15 nm and ~20 nm, respectively.

Higher quantities of mesopores in electrodes help in the switching behaviour for ions through the pores and hence increase rate capability during charging and discharging. Similar trends were observed for the supercapacitors using electrodes prepared from composite precursor made of biomass or pre-carbonized biomass added with CNT [33] and graphene [41], where the higher values of S_{meso}/S_{BET} values can lead to an improved performance of supercapacitors [42, 43].

3.2 Electrochemical properties

3.2.1 Cyclic Voltammetry

Figure 5 shows the comparative cyclic voltammograms recorded at room temperature at a scan rate of 1 mVs^{-1} for the cells namely ACM00, ACM10, ACM15 and ACM20. The cells for the electrode compositions ACM10, ACM15 and ACM20 exhibit quasi-rectangular shape of the voltammograms with higher voltammetric current as compared to the cell for the composition ACM00 and ACM05 (CV profile of the cell ACM05 is not shown here just to avoid overlapping with ACM00). This higher current and proper double layer formation can be accounted for the easy and fast electrolyte ion diffusion into the pores. In contrast to this, the deviation from rectangular shape and small voltammetric current in the CV profiles indicates that 5 wt. % of PPy in GMs is insufficient to produce ACMs that can have sufficient pores to transport the electrolyte ions.

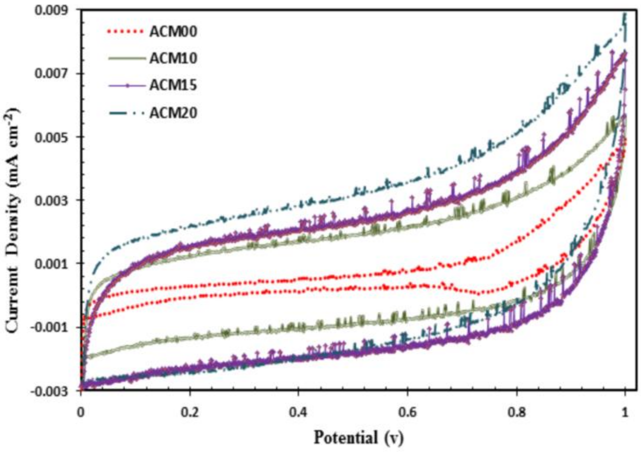

Figure 5. Cyclic voltammograms of ACM00, ACM10, ACM15 and ACM20 electrodes recorded at 1mVs^{-1}.

The reversible humps appearing in voltammogram in the voltage region above 0.8 V for the ACM00 electrode may be associated with the impurities in the ACM00 or the reaction of the electrolyte with the functional groups on the carbon surface.

The voltammograms show a typical variation in their shapes and areas for all the cells as the scan rate increases from 1 to 100 mVs^{-1} (not shown here). The specific capacitance values of the cells estimated from these voltammograms are plotted in Figure 6 as a function of scan rate. It can be observed that the specific capacitance values for ACM15 and ACM20 cells are consistently higher than the other cells throughout the whole scan rate region. This result indicates that the ACM15 and ACM20 possess the optimum pore networks, as evidently shown by the higher ratios of mesopore volume to micropore volume, which are more compatible with the ion size for the most efficient adsorption, thereby enhancing the gravimetric capacitance [44, 45]. Furthermore, a decay of 40 to 50 % from its maximum value in the specific capacitance has been observed for all the cells and this is comparable to the values reported in the literature for carbon based supercapacitors [46]. The decrease in capacitance at higher scan rates is common for carbon based supercapacitors because at this rate ion did not have sufficient available time to diffuse and reside inside the smallest inner pores within the electrodes.

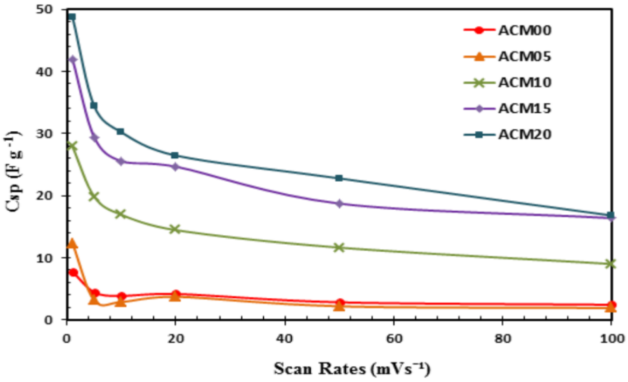

Figure 6. Variation of the specific capacitance with scan rates for ACM00, ACM05, ACM10, ACM15 and ACM20 electrodes.

3.2.2 Electrochemical Impedance Spectroscopy

As shown in Figure 7 (a and b), the Nyquist plots for all ACMs cells exhibit the typical features of EDLCs with porous electrodes. The plots show a resistive behaviour represented by a semicircle at very high frequency region, a Warburg resistance represented by a line segment with a slope around 45° at high frequency, and a dominant capacitive behaviour represented by an almost vertical line at low frequency region. The line segment with a slope around 45° in the Nyquist plot is related to the diffusion of the ions into pores of the electrodes [21]. The length and slope of these segments were observed to change with the change in PPy content in the GMs. It can be observed that all the compositions of the electrodes i.e., ACM05, ACM10, ACM15 and ACM20 (Nyquist plot for ACM05 is not shown here to avoid overlapping) exhibit a shorter Warburg length and Warburg slope closer to 45° slope line compared with the ACM00 electrode, with ACM15 electrode exhibiting the shortest length. This demonstrates that in this cell a very less resistance was encountered by the ions during their transport into the pore networks in the electrodes Figure 7 (b).

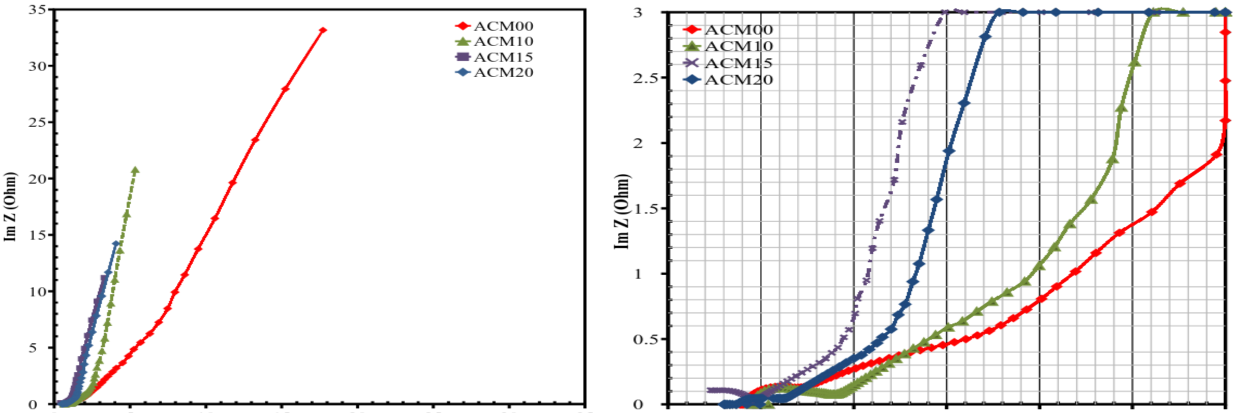

Figure 7. Nyquist plots for ACM00, ACM10, ACM15 and ACM20 cells.

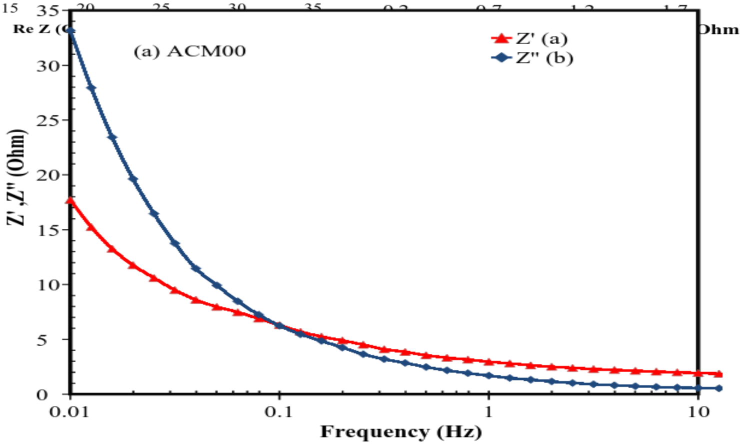

The power/rate capability of the

supercapacitors is determined by the equivalent series resistance (ESR), which is an estimation of the overall resistance present in the supercapacitors. The ESR is the contributions from the electrolyte resistance (which should be the same for all the samples), electrical resistance of the electrode (which should be the highest in the least dense or the most activated sample), and contact resistance of the interface between active electrode material and current collector. The ESR values determined from impedance spectra (Figure 7 (b)) for the ACM00, ACM05, ACM10, ACM15 and ACM20 cells are 2.15, 2.13, 2.10, 1.10 and 1.50 Ω, respectively. It can be noticed that the electrodes, ACM05, ACM10, ACM15 and ACM20 have lower ESR values than that of the ACM00 cell, and being the lowest for the electrode ACM15. The reason for this lowering in ESR values may be due to the relatively easy and efficient diffusion of electrolyte ions into the porous network of the cells ACM05, ACM10, ACM15 and ACM20 and caused by the addition of PPy.

Figure 8. Bode plot forACM00 electrode.

The rate performance of the device can also be discussed in terms of characteristic response time τ_o. The smaller the response time, the higher the rate capability of the device. The response time τ_o is the reciprocal of the response or resonant frequency, f_o which is determined from the point of intersection of real and imaginary parts of impedance, *Z* (i.e. Z' and Z"), plotted as a function of log of frequency, referred as Bode plot [47]. Figure 8 shows the typical Bode plot for the cell ACM00. The values of characteristic response time τ_o, determined from Bode plots for the ACM00, ACM05, ACM10, ACM15 and ACM20 cells, are found to be ~ 11, 10, 10, 8, and 9 s, respectively. The lowest value of τ_o for the electrode ACM15 shows that it offers the best power capability as compared to the all compositions of the electrodes.

Figure 9 shows variation of C_{sp} as a function of increasing frequency. It can be noticed that a decrease in the value of C_{sp} occurs with increasing frequency, which may be due to the fact that at higher frequency the time for the electrolyte ions entering the pores is shorter, so that the double layer formation is prevented in this frequency region. Comparison of the frequencies (f_p) at which the C_{sp} drops by 50 % from their highest values for the ACM00 and

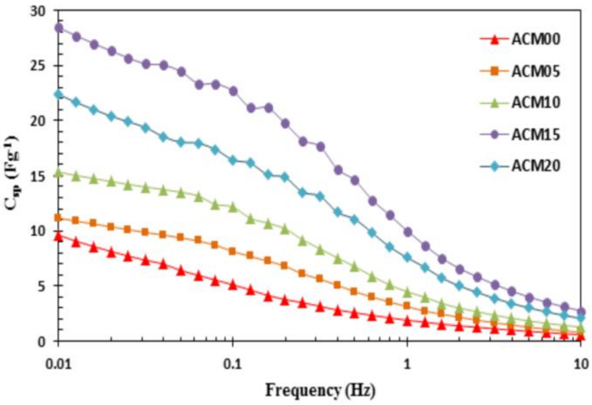

ACM05 cells, respectively, shows that the later cell has a higher f_p value and hence it has a better frequency response than the former cell (Figure 9). Further improvement in the frequency response is observed for ACM10 and ACM15 cells but not for the ACM20 cell, indicating a rejection of excessive quantity of PPy added to the GMs. This improved frequency response as well as the ESR and C_{sp} values, particularly for the ACM15 cell, was achieved, most likely due to a greater ionic mobility in the pores of electrodes because pore sizes and structure are compatible with the electrolyte ionic size. These results suggest that SACG added with a content of ~ (15-20) wt. % of PPy could be an optimum weight ratio of PPy to SACG for composite GMs to produce ACMs electrodes with optimum pores size and structure for supercapacitor application [8, 42].

Figure 9. Specific capacitance as a function of frequency for ACM00, ACM05, ACM10, ACM15 and ACM20 electrodes.

3.2.3 Galvanostatic Charge-Discharge

The galvanostatic charge-discharge (GCD) measurements were carried out at constant current density of 1 Ag^{-1} within the same voltage range as for cyclic voltammetry measurements. As shown in Figure 10 the GCD curves for all the ACM cells containing PPy were recorded in the potential range of 0 – 1 V and at a current density of 10 $mAcm^{-2}$. Except for the ACM00 electrode based cell, the all cells show similar and almost symmetrical triangular curves with an approximately linear variation of voltage as a function of time during charge and discharge. This feature of the curves is typical for carbon-based supercapacitors, and the data show that the ACMs (doped with varying amount of PPy) electrodes based cells have a good supercapacitive performance. Further, it can be observed from Figure 10 that the curves for the ACM15 and ACM20 cells show significantly higher charge and discharge times, which possibly result from a higher number of electrons and electrolyte ions participating in the charge and discharge processes of these electrodes compared to the ACM00, ACM05 and ACM10 electrodes. This further confirms that the higher percentage of PPy in GMs can produce better electrodes for supercapacitor application as supported by the results obtained by the EIS and CV methods [8, 42].

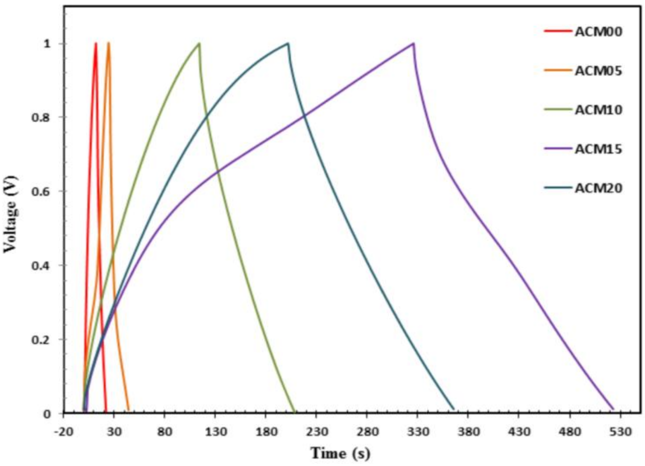

Figure 10. Charge-discharge curves of ACM00, ACM05, ACM10, ACM15 and ACM20 electrodes recorded at a current density of 10 mA cm^{-2}.

A slight voltage drop at the beginning of the discharge curve that appears in all GCD curves (Figure. 10) is associated with the ESR of the cells and could be calculated using ESR = $iR_{drop}/2I$, where iR_{drop} is defined as the electrical potential difference at the beginning of the discharge curves, and i is the discharge current. The calculated ESR values for the ACM00, ACM05, ACM10, ACM15 and ACM20 cells are 6.37, 2.78, 3.40, 1.95 and 1.05 **Ω**, respectively. These values are as good as reported in the literature for carbon based electrodes derived from various biomasses and their processed bi-product wastes [3, 21, 48-51]. This indicates that the addition of PPy in GMs decreases the ESR values of the cells. The reduced ESR values could improve the power performance of the cells because the power is inversely proportional to ESR.

3.2.4 Ragone Plots

Plotting specific power (P) of the cells against its specific energy (E) is a good approach to estimate the deviation from its ideal behaviour (Figure 11). Despite from the cells comprising of ACM00 and ACM05 electrodes, all the cells fabricated with ACM10, ACM15 and ACM20 electrodes show typical knee shaped patterns which approximately exhibit ideal characteristics of the device. The maximum values of specific energy and specific power of all cells are presented in Table 3. It can be noticed that the cell ACM15 and ACM20 offer maximum values of specific energy and specific power ranging from ~ 3 to 6 Wh kg^{-1} and from ~ 96 to 98 W kg^{-1}, respectively. The trend of these results (specific energy and specific power) is strongly dependent on the pore characteristics of the electrodes of the cells, and is similar to the one typically found for carbon based supercapacitors reported elsewhere [6, 45, 50, 52-57].

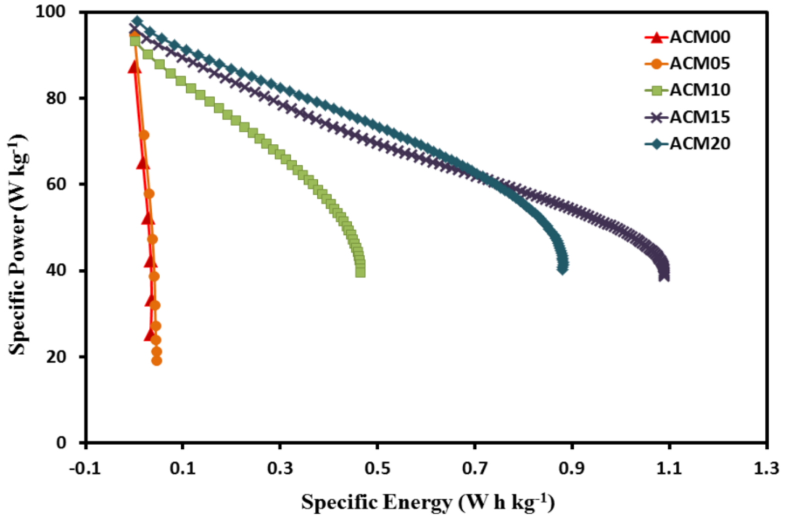

Figure 11. Specific power against specific energy or Ragone plots, for all the cells (ACM00, ACM05, ACM10, ACM15 and ACM20).

Table 3. Specific capacitance for ACMs evaluated from EIS, CV, GCD techniques.

	C_{sp}(Fg^{-1})	C_{sp}(Fg^{-1})	C_{sp}(Fg^{-1})	E(Wh kg^{-1})	P(W kg^{-1})	
ACM00	9.60	7.80	2.09	2.43	87.37	1.7124
ACM05	11.16	12.32	3.97	2.63	94.57	1.2821
ACM10	15.31	27.89	19.97	2.59	93.29	0.2567
ACM15	28.42	41.97	41.45	2.67	96.19	2.4514
ACM20	22.38	48.76	33.66	5.99	97.98	1.1850

4. CONCLUSIONS

GMs prepared from KOH treated SACG derived from fibres of OPEFB added with 0 to 20 wt. % of PPy were carbonized and activated into the ACMs electrodes for their application in supercapacitors. The addition of PPy to the precursor GMs was found to affect the structure, microstructure, and pore structure of the electrodes. Likewise, a significant improvement in the specific capacitance (20-50 F g^{-1}), specific energy (3-6 Wh kg^{-1}) and specific power of the supercapacitors were achieved for ACMs electrodes containing ~ 15 to 20 wt. % of PPy with respect to the GMs electrodes (without PPy) exhibiting the corresponding values of ~ (2-10) F g^{-1}, 2 Wh kg^{-1}, and 87 W kg^{-1}. It can be concluded that SACG is compatible to be mixed with PPy and an appropriate amount of PPy can significantly improve the performance of supercapacitor electrodes prepared from the composite GMs containing SACG and PPy.

ACKNOWLEDGEMENTS
The authors are grateful to the research grants from MOE (ERGS/1/2012/STG05/UKM/01/2), (FRGS/2/2013/ST05/UKM/01/1), UKM (UKM-DIP-2014-027, UKM-Industri-2013-026), MOSTI (03-01-02-SF1118) and the support of CRIM of UKM with instruments. The authors also thank to Mr.

Saini for help with the laboratory work and for the kind collaborative work of Department of Physics and Astrophysics, University of Delhi, India.

References

1. B. E. Conway, Electrochemical Supercapacitors: Scientific Fundamentals and Technological Applications, Kluwer Academic/Plenum Publishers, New York, 1999.
2. G. Yu, X. Xie, L. Pan, Z. Bao, Y. Cui, *Nano Energy,* 2 (2013) 213.
3. N. H. Basri, M. Deraman, S. Kanwal, I. A. Talib, J. G. Manjunatha, A. A. Aziz, R. Farma, *Biomass Bioenergy,* 59 (2013) 370.
4. A. S. Aricò, P. Bruce, B. Scrosati, J. M. Tarascon, W. van Schalkwijk, *Nat. Mater.,* 4 (2005) 366.
5. B. Kang, G. Ceder, *Nature*, 458 (2009) 190.
6. P. Simon, Y. Gogotsi, *Nat. Mater.*, 7 (2008) 845.
7. H. Tamai, M. Hakoda, T. Shiono, H. Yasuda, *J. Mater. Sci.,* 42 (2007) 1293.
8. J. Zhang, L. Bin Kong, H. Li, Y.C. Luo, L. Kang, *J. Mater. Sci.,* 45 (2010) 1947.
9. L. Wei, M. Sevilla, A.B. Fuertes, R. Mokaya, G. Yushin, *Adv. Funct. Mater.,* 22 (2012) 827.
10. J. Janata, M. Josowicz, *Nat. Mater.,* 2 (2003) 19.
11. T. V. Vernitskaya, O.N. Efimov, *Russ. Chem. Rev.,* 66 (1997) 443.
12. G. A. Snook, P. Kao, A.S. Best, *J. Power Sources,* 196 (2011) 1.
13. E. Taer, M. Deraman, I. A. Talib, A. A. Umar, M. Oyama, R. M. Yunus, *Curr. Appl. Phys.*, 10 (2010) 1071.
14. N. S. M. Nor, M. Deraman, R. Omar, E. Taer, R. Farma, N. H. Basri, B. N. M. Dolah, *AIP Proc.*, 1586 (2014) 68.
15. E. Taer, M. Deraman, I. A. Talib, A. Awitdrus, S. A. Hashmi, A. A. Umar, *Int. J. Electrochem. Sci.* 6 (2011) 3301.
16. X. Li, W. Xing, S. Zhuo, J. Zhou, F. Li, S. Z. Qiao, G. Q. Lu, *Bioresour. Technol.,* 102 (2011) 1118.
17. J. M. V. Nabais, J. G. Teixeira, I. Almeida, *Bioresour. Technol.,* 102 (2011) 2781.
18. A. Elmouwahidi, Z. Zapata-Benabithe, F. Carrasco-Marín, C. Moreno-Castilla, *Bioresour. Technol.,* 111 (2012) 185.
19. R. Farma, M. Deraman, Awitdrus, I. A. Talib, R. Omar, J. G. Manjunatha, M. M. Ishak, N. H. Basri, B. N. M. Dolah, *Int. J. Electrochem. Sci.,* 8 (2013) 257.
20. M. Suleman, Y. Kumar, S. A. Hashmi, *J. Solid State Electrochem.,* 19 (2015) 1347.
21. R. Farma, M. Deraman, A. Awitdrus, I. A. Talib, E. Taer, N. H. Basri, J. G. Manjunatha, M. M. Ishak, B. N. M. Dollah, S. A. Hashmi, *Bioresour. Technol.,* 132 (2013) 254.
22. E. Frackowiak, Q. Abbas, F. Béguin, *J. Energy Chem.,* 22 (2013) 226.
23. K. C. Tsay, L. Zhang, J. Zhang, *Electrochim. Acta,* 60 (2012) 428.
24. W. Lu, D. D.L. Chung, *Carbon,* 39 (2001) 39.
25. M. Deraman, M. P. Ismail, M. M. Said, *J. Mater. Sci. Lett.,* 14 (1995) 781.
26. Review of the Malaysian Oil Palm Industry (ISSN: 1511 – 7448), 2003.
27. M. Deraman, *J. Phys. D. Appl. Phys.,* 27 (1999) 1060.
28. M. Deraman, R. Omar, S. Zakaria, I. R. Mustapa, M. Talib, N. Alias, *J. Mater. Sci.,* 37 (2002) 3329.
29. M. Deraman, R. Omar, A. G. Harun, *J. Mater. Sci. Lett.,* 17 (1998) 2059.
30. M. Deraman, S. Zakaria, R. Omar, A. A. Aziz, *Jpn. J. Appl. Phys.,* 39 (2000) 1236.
31. M. Deraman, S. Zakaria, S. Murshidi, *Jpn. J. Appl. Phys.,* 40 (2001) 3311.
32. K. S. W. Singh, D. H. Everett, R. A. W. Hull, L. Moscou, R. A. Pierotti, J. Rouquerol, T. Siemieniewska, *Pure Appl. Chem.,* 57 (1985) 603.

33. C. Portet, P. L. Taberna, P. Simon, E. Flahaut, C. Laberty-Robert, *Electrochim. Acta*, 50 (2005) 4174.
34. L. Chunlan, X. Shaoping, G. Yixiong, L. Shuqin, L. Changhou, *Carbon*, 43 (2005) 2295.
35. C. E. Byrne, D. C. Nagle, *Carbon*, 35 (1997) 259.
36. N. Su, H. B. Li, S. J. Yuan, S. P. Yi, E. Q. Yin, *Express Polym. Lett.*, 6 (2012) 697.
37. Z. Q. Li, C. J. Lu, Z. P. Xia, Y. Zhou, Z. Luo, *Carbon*, 45 (2007) 1686.
38. M. Deraman, I. A. Talib, M. Ramli Omar, H. H. J. Jumali, E. Taer, M. M. Saman, *Sains Malays*, 39 (2010) 83.
39. S. Zakaria, R. Roslan, U. A. Amran, C. C. Hua, S. B. Bakaruddin, *Sains Malays*, 43 (2014) 429.
40. J. Yang, K. Qiu, *Chem. Eng. J.*, 165 (2010) 209.
41. L. Zhang, F. Zhang, X. Yang, G. Long, Y. Wu, T. Zhang, K. Leng, Y. Huang, Y. Ma, A. Yu, Y. *Chen, Sci. Rep.*, 3 (2013) 1408.
42. A. G. Pandolfo, A. F. Hollenkamp, *J. Power Sources*, 157 (2006) 11.
43. S. Y. Zhou, X. H. Li, Z. X. Wang, H. J. Guo, W. J. Peng, *J. Cent. South Univ. Technol.*, 15 (2008) 674.
44. C. Largeot, C. Portet, J. Chmiola, P. L. Taberna, Y. Gogotsi, P. Simon, *J. Am. Chem. Soc.*, 130 (2008) 2730.
45. Awitdrus, M. Deraman, I. A. Talib, R. Farma, R. Omar, M. M. Ishak, N. H. Basri, *Adv. Mater. Res.*, 501 (2012) 13.
46. S. A. Hashmi, A. Kumar, S. K.Tripathi. *J. Phys. D. Appl. Phys.*, 40 (2007) 6527.
47. J. R. Miller, *Proc. Eighth International Seminar on Double layer Capacitors and Similar Energy Storage Devices*, 1998.
48. E. Taer, M. Deraman, I. A. Talib, S. A. Hashmi, A. A. Umar, *Electrochim. Acta*, 56 (2011) 10217.
49. B. N. M. Dolah, M. Deraman, M. A. R. Othman, R. Farma, E. Taer, Awitdrus, N.H. Basri, I. A. Talib, R. Omar, N.S.M. Nor, *Mater. Res. Bull.*, 60 (2014) 10.
50. N. S. M. Nor, M. Deraman, R. Omar, Awitdrus, R. Farma, N. H. Basri, B.N. Mohd Dolah, N.F. Mamat, B. Yatim, M. N. M. Daud, *Energy*, 79 (2015) 183.
51. M. Biswal, A. Banerjee, M. Deo, S. Ogale, *Energy Environ. Sci.*, 6 (2013) 1249.
52. Q. Xiao, X. Zhou, *Electrochim. Acta*, 48 (2003) 575.
53. M. Deraman, R. Daik, S. Soltaninejad, N. S.M. Nor, Awitdrus, R. Farma, N. F. Mamat, N. H. Basri, M. A. R. Othman, Adv. Mat. Res., 1108 (2015) 1-7.
54. N. S. M. Nor, M. Deraman, N. H. Basri, B. N. M. Dollah, R. Omar, S. Soltaninejad, R. Daik and M. D. Norizam, Adv. Mat. Res., 1112 (2015) 303-307.
55. M. Deraman, N. S. M. Nor, N. H. Basri, B. N. M. Dollah, S. Soltaninejad, R. Daik, R. Omar, M. A. Hashim and M. A. R. Othman, Adv. Mat. Res., 1112 (2015) 231-235.
56. S. Soltaninejad, M. Deraman, R. Daik, N. S. M. Nor, B. N. M. Dollah, N. H. Basri, Adv. Mat. Res., 1112 (2015) 299-302.
57. M. M. Ishak, M. Deraman, B. N. M. Dolah, M. A. R. Othman, R. Omar, N. H. Basri, N. S. M. Nor, E. Taer, R. Farma, A. A. Aziz, Adv. Mat. Res., 1112 (2015) 308-312.